ELECTRONIC SEISMOLOGIST

A Suite of Exercises for Verifying Dynamic Earthquake Rupture Codes

by Ruth A. Harris, Michael Barall, Brad Aagaard, Shuo Ma, Daniel Roten, Kim Olsen, Benchun Duan, Dunyu Liu, Bin Luo, Kangchen Bai, Jean-Paul Ampuero, Yoshihiro Kaneko, Alice-Agnes Gabriel, Kenneth Duru, Thomas Ulrich, Stephanie Wollherr, Zheqiang Shi, Eric Dunham, Sam Bydlon, Zhenguo Zhang, Xiaofei Chen, Surendra Nadh Somala, Christian Pelties, Josué Tago, Victor Manuel Cruz-Atienza, Jeremy Kozdon, Eric Daub, Khurram Aslam, Yuko Kase, Kyle Withers, and Luis Dalguer

ABSTRACT

We describe a set of benchmark exercises that are designed to test if computer codes that simulate dynamic earthquake rupture are working as intended. These types of computer codes are often used to understand how earthquakes operate, and they produce simulation results that include earthquake size, amounts of fault slip, and the patterns of ground shaking and crustal deformation. The benchmark exercises examine a range of features that scientists incorporate in their dynamic earthquake rupture simulations. These include implementations of simple or complex fault geometry, off-fault rock response to an earthquake, stress conditions, and a variety of formulations for fault friction. Many of the benchmarks were designed to investigate scientific problems at the forefronts of earthquake physics and strong ground motions research. The exercises are freely available on our website for use by the scientific community.

INTRODUCTION

Dynamic (also known as spontaneous) earthquake rupture codes are computational tools that are used to understand the physical behavior of earthquakes and how earthquakes interact, on short time scales, with the earth that surrounds them. These codes implement friction on the faults and solve the equations of motion, including the effects of inertia. The codes allow for interactions between the seismic waves generated by an earthquake source and the earthquake source itself, so that the behavior of a simulated earthquake is not predetermined but instead is a result of the physical conditions at the start of the earthquake simulation, along with the time-dependent processes that occur during earthquake rupture.

Dynamic earthquake rupture codes require a number of initial assumptions and produce a variety of results (Fig. 1). The assumptions include the geometry of the faults, the initial stress conditions in the rocks before an earthquake, and the rocks' properties including their shear-wave and compressional-wave velocities and densities along with the information about whether or not the rocks deform elastically. The assumptions also include a relation between fault stresses and slip (a friction law) that governs how, when, and where fault sliding occurs. Results produced by dynamic rupture codes include spatial and temporal evolution of slip and stresses on the faults (Fig. 2), time-dependent Earth motions associated with the radiated seismic waves (Fig. 3), and other outcomes such as determinations of radiated energy and energy dissipation due to friction and yielding of the rocks near the faults.

These types of codes are similar to the more common kinematic earthquake rupture simulation codes, in their need for information about the fault geometry and off-fault rock properties. However, in contrast to ruptures produced in dynamic earthquake simulations, kinematic earthquake rupture simulations require the slip and time evolution of the rupture process to be prescribed, and kinematic rupture simulations do not necessarily produce results that are consistent with rock physics. Kinematic rupture simulations also do not allow for feedback between a propagating earthquake rupture and the dynamic stress field associated with the radiated seismic waves propagating through the surrounding rocks.

Dynamic earthquake rupture simulations have many desirable qualities, such as directly linking models of frictional sliding on a fault surface to earthquake rupture behavior and the resulting radiated seismic waves that produce ground shaking. The primary difficulty in applying them to advance our understanding of earthquake rupture processes is our inability to validate such models, due to our lack of knowledge about the fine-scale details of the state of stress on and near crustal faults and faults' constitutive behavior under realistic conditions. To address this problem, more than a decade ago we formed the Southern California Earthquake Center-U.S. Geological Survey (SCEC-USGS) dynamic rupture code validation group (Harris and Archuleta, 2004), which is an international collaboration to verify and validate computer codes used to simulate earthquakes as spontaneous dynamic ruptures. While our

 doi: 10.1785/0220170222

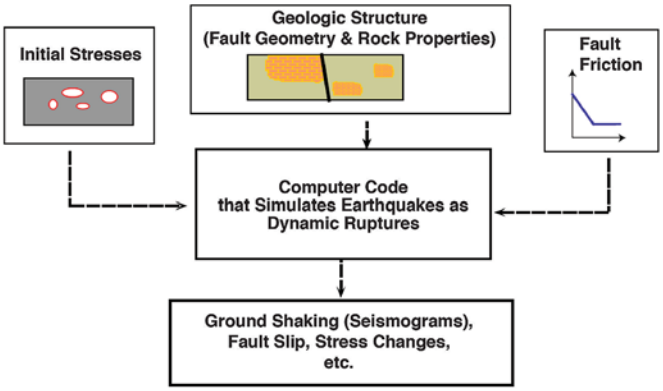

▲ **Figure 1.** Key ingredients of a dynamic (spontaneous) earthquake rupture simulation include the initial stresses on and off the faults, the geometry of the faults, the properties of the nearby rocks, including their densities and compressional and shear-wave velocities, along with information about how the rocks deform in response to Earth movements (e.g., if they deform elastically or inelastically), and a formulation that describes how fault friction works. Fault friction determines if, where, and when sudden fault sliding (the earthquake) can occur. These assumptions are incorporated as the starting conditions in a computer code that simulates the evolving earthquake source and the earthquake source's interactions with the rocks that surround the faults. Results include time-dependent ground shaking, fault slip, and other information, examples of which are shown in Figures 2 and 3. Figure modified from Harris (2004).

ultimate goal remains validation of these numerical models, in the intervening time we have focused on the intermediate goal of testing whether our codes produce the same results given the same set of assumptions. To this end, we have successfully verified that about a dozen different finite-difference, spectral element, and finite-element computer codes (Table 1) that simulate dynamic earthquake ruptures produce essentially the same results for a broad range of assumptions, spanning vertical, dipping, planar, nonplanar, and intersecting fault geometries, homogeneous and heterogeneous linear elastic and viscoelastoplastic rock rheology, heterogeneous stress conditions, and various fault friction models, all of which are important attributes for real earthquakes.

THE DYNAMIC (SPONTANEOUS) EARTHQUAKE RUPTURE BENCHMARK EXERCISES

Our group has created and used a suite of exercises designed to verify that dynamic (spontaneous) earthquake rupture codes produce the same results given the same assumptions about elastodynamics and fault constitutive behavior. In developing our suite of code verification exercises (Table 2), our group has explored scientific questions, particularly how geological and geophysical evidence of fault complexity and rock response affect the behavior of earthquake rupture. Whereas the answers to some of our ongoing science questions are not yet within reach due to both the current limitations of computational hardware and a lack of observational data, our benchmark exercises have been designed so that the simulations can be conducted on currently available high-performance computational platforms, and the results include seismograms and other products that can be compared with "real Earth" types of data.

Our exercises follow our motto of incrementally adding complexity. This has helped us detect which features of each of our benchmarks and codes might be producing challenges, particularly when discrepancies arise among the codes' results. Although it is often tempting to leap from simple to complex simulation settings, we have rarely observed this to be a good strategy for either our or others' code-testing exercises. Instead, the slow but steady approach has worked best.

In the course of our exercises, we explored earthquake-science questions. These have sometimes required computational solutions for simulating the nature of earthquake nucleation and cessation. As we moved forward through our benchmark suite, the nucleation and cessation assumptions for our simulations have evolved, from simple and easy to implement descriptions to those with slightly more complexity that are more computationally robust, and perhaps more realistic. For more detailed discussions about the techniques for nucleating dynamic earthquake ruptures, the readers are referred to Andrews (2004), Bizzarri (2010), and Galis *et al.* (2015).

We now present the benchmark exercises along with some of their scientific motivations. The detailed specifications for each of these code-verification benchmark exercises is available on our website (see Data and Resources), so that others in the scientific community may independently test their own dynamic rupture codes. Information about some of our older benchmarks is also available in our earlier group publications (Harris *et al.*, 2009, 2011).

TPV3 and TPV4

Our group's first benchmark exercises were TPV1 and TPV2 (The Problem Version 1 and The Problem Version 2), but these were primarily for training, and they were superseded by TPV3 and TPV4 (The Problem Version 3 and The Problem Version 4). TPV3 and TPV4 are our group's simplest and first successful forays into dynamic (spontaneous) rupture code verification. In TPV3, our group simulated the case of a rupture that is artificially nucleated in the middle of a vertical strike-slip rectangular fault with uniform initial stresses (outside the nucleation zone), then spontaneously propagates until it reaches strong regions at the sides and bottom of the fault. The rock surrounding the fault responds elastically, and it has a homogeneous velocity and density structure; the fault friction is slip weakening (Ida, 1972; Palmer and Rice, 1973; Andrews, 1976; Day, 1982). For TPV3, the model is a full-space. For TPV4, the model is a half-space, the fault intersects the Earth's surface, and the earthquake rupture spontaneously propagates up to the Earth's surface. These two benchmark exercises were conducted before our group had a code-verification website, so they are mentioned here primarily for historical reasons. TPV3 was also the basis for a quantitative study that established the criteria for proper grid resolution in dynamic rupture simula-

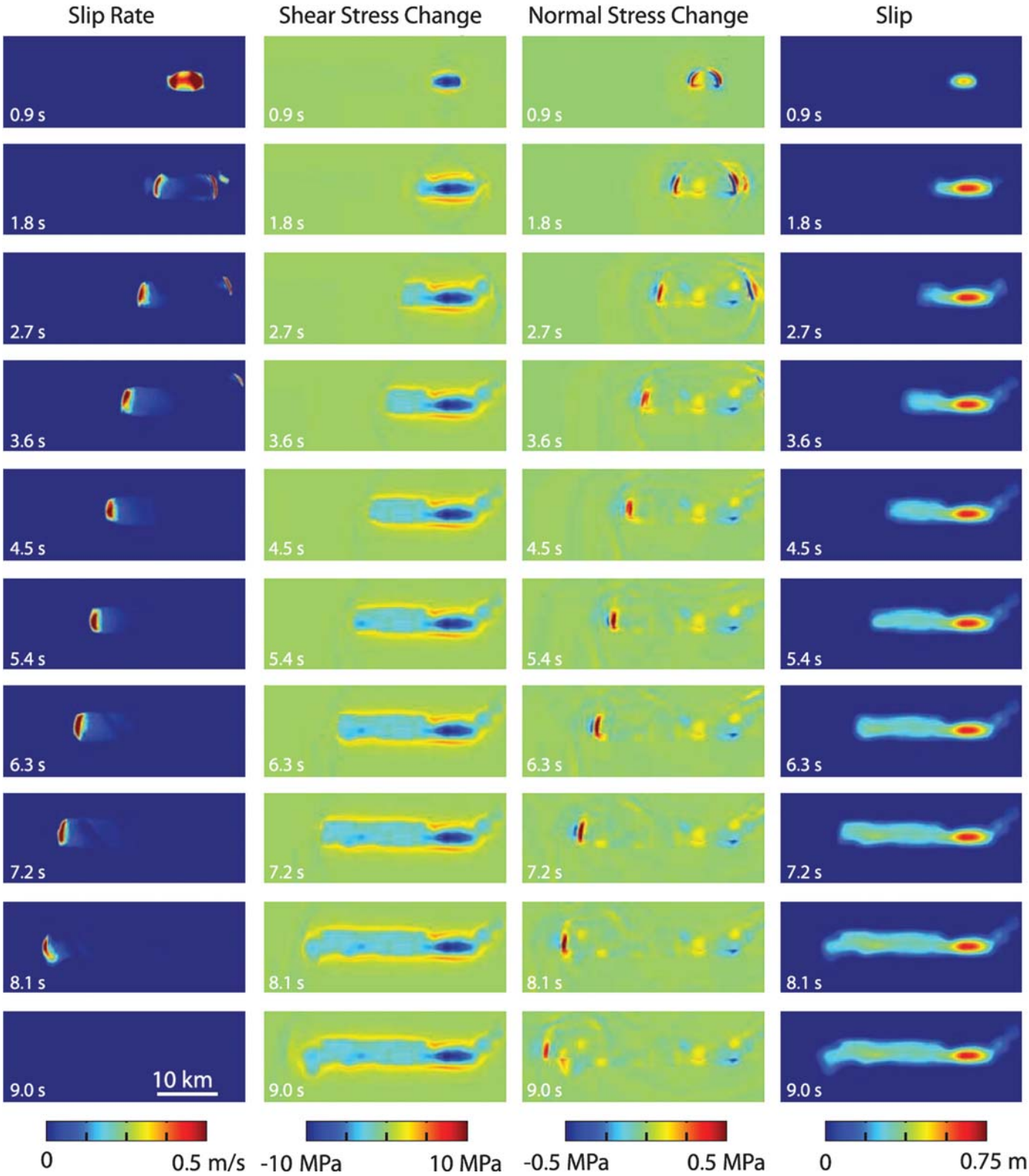

▲ **Figure 2.** Example of results produced using dynamic (spontaneous) earthquake rupture simulation code MAFE (Ma *et al.*, 2008). Time-dependent pattern of an earthquake rupture on a planar vertical strike-slip fault surface. The simulated earthquake, in this case the Ma *et al.* (2008)-favored model of the 2004 **M** 6.0 Parkfield, California, earthquake, was nucleated at 0.0 s on the fault surface, centered at a depth of 8.1 km. The subsequent dynamic, spontaneously propagating rupture is shown in figure 5 of Ma *et al.* (2008) (reproduced here) as a time-evolving pattern of slip rate, shear stress change, normal stress change, and slip on the fault surface, in snapshots starting at 0.9 s after nucleation.

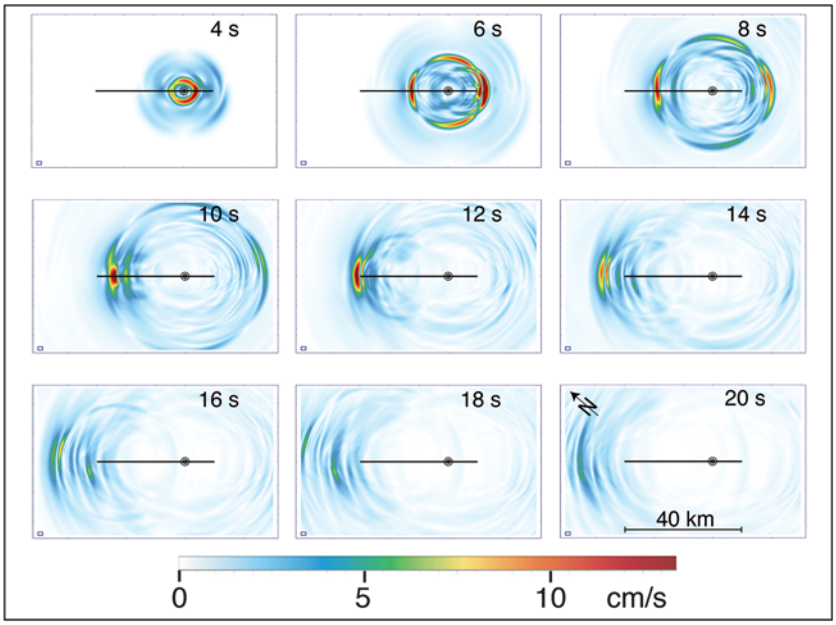

▲ **Figure 3.** Example of results produced using dynamic (spontaneous) earthquake rupture simulation code FaultMod (Barall, 2009). Using the same 2004 **M** 6 Parkfield earthquake parameters (from Ma *et al.*, 2008) as were used for Figure 2, the simulated earthquake rupture generates ground shaking. The magnitude of the 3D ground-shaking velocity at the Earth's surface is shown in snapshots starting at 4 s after nucleation. The black line shows the projection of the fault surface where it intersects the Earth's surface. The small circle is the simulated earthquake's epicenter.

tions (Day *et al.*, 2005) along with additional code performance metrics (e.g., Moczo *et al.*, 2007; Tago *et al.*, 2012). For the rest of the exercises described in this article, unless noted otherwise, the rock surrounding the fault(s) responds elastically and has a homogeneous velocity and density structure, and the fault friction weakens with increasing fault slip (slip weakening).

TPV5

This is our first group exercise that is posted on our group's website (see Data and Resources). TPV5 (Fig. 4) is considered as one of our benchmark classics, and it is frequently used by those who are checking the potential viability of a new dynamic (spontaneous) rupture code, or a newly modified code. The rupture is artificially nucleated in the middle of a vertical strike-slip rectangular fault that intersects the Earth's surface. The rupture then spontaneously propagates to the left, right, and bottom edges of the fault where it is forced to stop abruptly at a hard border, and up to the Earth's surface. The rupture encounters two patches on the fault surface, one with a higher initial shear stress than the rest of the active fault surface, one with a lower initial shear stress, and each of these patches mildly affects the propagating rupture. TPV205 is the same as this exercise, except that TPV205 is a convergence test and requests that the simulations be repeated multiple times, with each simulation using a different discretization size in the computational mesh. TPV205 examines the codes' capabilities to produce the same results using different mesh discretization sizes that range over two orders of magnitude.

TPV6 and TPV7

These are our first bimaterial exercises, where the elastic moduli of the rocks on one side of the fault differ from the elastic moduli of the rocks on the other side of the fault. The material contrast (Fig. 5) is stronger for TPV6 than it is for TPV7. The rupture is artificially nucleated in the middle of a vertical strike-slip rectangular fault with uniform initial stresses (outside the nucleation zone) that intersects the Earth's surface. The rupture then spontaneously propagates to the left, right, and bottom edges of the fault where it is stopped by strong fault regions, and up to the Earth's surface. The rock responds elastically and the fault friction is slip weakening. One of these two exercises, TPV6, is well posed, in the sense defined by Ranjith and Rice (2001), meaning that the results will converge, rather than keep changing as the computational mesh's discretization size decreases.

TPV8 and TPV9

These two exercises are the first in a sequence leading up to our extreme ground-motion benchmarks, TPV12 and TPV13. TPV8 and TPV9 use a vertical rectangular fault that intersects the Earth's surface. The two exercises are identical except that TPV8 is a strike-slip fault and TPV9 is a dip-slip fault. Vertical dip-slip faults are uncommon in nature, but TPV9 was nonetheless a useful step toward our goal of simulating extreme ground motion. The initial shear and normal stresses on the fault vary linearly with depth and are chosen to produce a subshear rupture (i.e., a rupture that propagates at less than the shear-wave velocity of the surrounding rock). For both benchmarks, the rupture is artificially nucleated near the bottom of the vertical strike-slip rectangular fault that intersects the Earth's surface. The rupture then spontaneously propagates to the left, right, and bottom edges of the fault where it is stopped by strong fault regions, and up to the Earth's surface.

TPV10 and TPV11

These two exercises are the next in the sequence leading up to our extreme ground-motion benchmarks. They are our first benchmarks with a nonvertical fault. TPV10 and TPV11 both use a 60° dipping dip-slip normal fault that intersects the Earth's surface, and initial shear and normal stresses on the fault that vary linearly with depth. The two exercises are identical, except that TPV10 has a higher static coefficient of friction than TPV11. The initial stresses and friction parameters lead to a subshear (slower than the rock's shear-wave velocity) rupture in TPV10, and a supershear (faster than the rock's

Table 1
List of Many of Our Group's Dynamic Earthquake Rupture Codes

Code Name	Code Type	References	Notes	Code Availability
AWP-ODC	Finite difference	Roten *et al.* (2016) and Dalguer and Day (2007)		Contact author Roten
beard	Discontinuous Galerkin finite element	Kozdon *et al.* (2015)		Contact author Kozdon
CG-FDM	Finite difference	Zhang *et al.* (2014)		Contact author Zhang
EqSim	Finite element	Aagaard *et al.* (2001)	Superseded by PyLith	
DFM	Finite difference	Day and Ely (2002)		Contact author Dalguer
DGCrack	Discontinuous Galerkin finite element	Tago *et al.* (2012)		Contact authors Tago or Cruz-Atienza
EQdyna	Finite element	Duan and Oglesby (2006)		Contact author Duan
FaultMod	Finite element	Barall (2009)		Contact author Barall
fdfault	Finite difference	Daub (2016)		Available at GitHub. See Data and Resources
Kase code	Finite difference	Kase and Kuge (2001)		Contact author Kase
MAFE	Finite element	Ma *et al.* (2008) and Ma and Andrews (2010)		Contact author Ma
PyLith	Finite element	Aagaard *et al.* (2013)		Available at CIG. See Data and Resources
SeisSol	Discontinuous Galerkin finite element	Pelties *et al.* (2012) and Pelties *et al.* (2014)		Available at GitHub. See Data and Resources
SESAME	Spectral element	Galvez *et al.* (2014)	Same as SPECFEM3D	
SORD	Finite difference	Ely *et al.* (2009) and Shi and Day (2013)		Contact author Shi
SPECFEM3D	Spectral element	Galvez *et al.* (2014)		Available at CIG. See Data and Resources
SPECFEM3D-old	Spectral element	Kaneko *et al.* (2008)	Superseded by SPECFEM3D	
WaveQLab3D	Finite difference	Duru and Dunham (2016)		Available at Bitbucket. See Data and Resources

shear-wave velocity) rupture in TPV11. The rupture is artificially nucleated near the bottom of the fault. The rupture spontaneously propagates to the left, right, and bottom edges of the fault where it is stopped by strong fault regions, and up to the Earth's surface. TPV210 is the same as TPV10 and examines the codes' capabilities to produce the same results irrespective of the mesh discretization details.

TPV12 and TPV13

These exercises are similar to TPV11, except that the initial stress conditions lead to fast rupture speed (supershear) and cause extreme ground shaking near the fault. In TPV12 the rock response is elastic, and in TPV13 the rock response assumes nonassociative Drucker–Prager plasticity with yielding in shear. These are our first exercises to include gravity, fluid pressure (which was assumed constant), and an initial stress tensor specified throughout the model volume (as opposed to specifying just the initial shear and normal stresses on the fault surface), all of which is compelled by the fact that TPV13 is our first exercise to use inelastic rock properties. The constant fluid pressure in particular was included to ensure that the stresses would be smaller than lithostatic values. Both TPV12 and TPV13 were designed to test the code that had been used by Andrews *et al.* (2007) to produce simulations of extreme ground motions near the proposed high-level nuclear waste repository at Yucca Mountain, Nevada (Andrews *et al.*, 2007), and work using these two benchmarks is published in Harris *et al.* (2011). TPV12 and TPV13 (Fig. 6) are provided in both 2D and 3D versions, and are two of our classic well-tested benchmark exercises that we recommend for new codes and for modelers who are using our benchmarks for the first time.

TPV14 and TPV15

These are the first nonplanar fault exercises. TPV14 is the case of a vertical right-lateral strike-slip branching fault, with a rightward branch that forms a 30° angle with the main fault (a releasing branch). TPV15 is the same as TPV14, except that TPV15 is a left-lateral strike-slip fault with a rightward branch (a restraining branch). The fault geometry for TPV15 is equivalent to a left branch in a right-lateral strike-slip fault, which is

Table 2
Features of the Benchmark Exercises

Exercise	3D or 2D	Friction*	Rock Structure†	Initial Stress‡	Geometry	Rock Response	Notes§
TPV3	3D	SW	Homog.	Homog., strike-slip	Vertical plane	Elastic	Full-space
TPV4	3D	SW	Homog.	Homog., strike-slip	Vertical plane	Elastic	Half-space
TPV5	3D	SW	Homog.	Two patches, strike-slip	Vertical plane	Elastic	Classic
TPV6	3D	SW	Bimaterial	Homog., strike-slip	Vertical plane	Elastic	Preferred bimaterial exercise
TPV7	3D	SW	Bimaterial	Homog., strike-slip	Vertical plane	Elastic	Rupture not well resolved
TPV8	3D	SW	Homog.	Depth-dep., strike-slip	Vertical plane	Elastic	
TPV9	3D	SW	Homog.	Depth-dep., dip-slip	Vertical plane	Elastic	
TPV10	3D	SW	Homog.	Depth-dep., dip-slip	Dipping plane	Elastic	Subshear
TPV11	3D	SW	Homog.	Depth-dep., dip-slip	Dipping plane	Elastic	Dip-slip supershear
TPV12	3D and 2D versions	SW	Homog.	Depth-dep., dip-slip	Dipping plane	Elastic	Classic ExGM supershear
TPV13	3D and 2D versions	SW	Homog.	Depth-dep., dip-slip	Dipping plane	Plastic	Classic ExGM supershear
TPV14	3D and 2D versions	SW	Homog.	Homog., strike-slip	Branched vertical fault	Elastic	Releasing branch
TPV15	3D and 2D versions	SW	Homog.	Homog., strike-slip	Branched vertical fault	Elastic	Restraining branch
TPV16	3D	SW	Homog.	Stochastic, strike-slip	Vertical plane	Elastic	
TPV17	3D	SW	Homog.	Stochastic, strike-slip	Vertical plane	Elastic	
TPV18	3D	SW	Homog.	Depth-dep., strike-slip	Branched vertical fault	Elastic	Releasing branch
TPV19	3D	SW	Homog.	Depth-dep., strike-slip	Branched vertical fault	Plastic	Releasing branch
TPV20	3D	SW	Homog.	Depth-dep., strike-slip	Branched vertical fault	Elastic	Restraining branch
TPV21	3D	SW	Homog.	Depth-dep., strike-slip	Branched vertical fault	Plastic	Restraining branch
TPV22	3D	SW	Homog.	Homog., strike-slip	Stepover in vertical fault	Elastic	Stress taper at base
TPV23	3D	SW	Homog.	Homog., strike-slip	Stepover in vertical fault	Elastic	Stress taper at base
TPV24	3D	SW	Homog.	Depth-dep., strike-slip	Branched vertical fault	Elastic	Releasing branch
TPV25	3D	SW	Homog.	Depth-dep., strike-slip	Branched vertical fault	Elastic	Restraining branch
TPV26	3D	SW	Homog.	Depth-dep., strike-slip	Vertical plane	Elastic	
TPV27	3D	SW	Homog.	Depth-dep., strike-slip	Vertical plane	Viscoplastic	

*SW, slip-weakening fault friction; RS-AL, rate–state fault friction with an ageing law; RS-SL-SRW, rate–state fault friction with a slip law with strong rate weakening; TP-RS-SRW, thermal pressurization with rate–state fault friction using a slip law with strong rate weakening.

†Rock structure includes material velocities and densities; homog., homogeneous.

‡Initial stress outside the nucleation zone; depth-dep., depth-dependent; heterog., heterogeneous; prop. to shear mod., proportional to shear modulus.

§ExGM, extreme ground motion.

(Continued next page.)

Table 2 (continued)
Features of the Benchmark Exercises

Exercise	3D or 2D	Friction*	Rock Structure†	Initial Stress‡	Geometry	Rock Response	Notes§
TPV28	3D	SW	Homog.	Regional stress tensor	Vertical plane + 2 protuberances	Elastic	
TPV29	3D	SW	Homog.	Regional stress tensor	Vertical plane with roughness	Elastic	Stochastic roughness
TPV30	3D	SW	Homog.	Regional stress tensor	Vertical plane with roughness	Viscoplastic	Stochastic roughness
TPV31	3D	SW	1D	Prop. to shear mod., strike-slip	Vertical plane	Elastic	Discontinuous 1D velocity structure
TPV32	3D	SW	1D	Prop. to shear mod., strike-slip	Vertical plane	Elastic	Continuous 1D velocity structure
TPV33	3D	SW	3D	Homog.	Vertical plane	Elastic	Stress taper at all sides
TPV34	3D	SW	3D	Prop. to shear mod., strike-slip	Vertical plane	Elastic	Truncated Imperial Valley 3D velocity model
TPV35	3D	SW	3D	Heterog., strike-slip	Vertical plane	Elastic	Parkfield
TPV101	3D	RS-AL	Homog.	Homog., strike-slip	Vertical plane	Elastic	Full-space
TPV102	3D	RS-AL	Homog.	Homog., strike-slip	Vertical plane	Elastic	Half-space
TPV103	3D	RS-SL-SRW	Homog.	Homog., strike-slip	Vertical plane	Elastic	Full-space
TPV104	3D	RS-SL-SRW	Homog.	Homog., strike-slip	Vertical plane	Elastic	Half-space
TPV105	2D	TP-RS-SRW	Homog.	homog., strike-slip	2D in-plane	Elastic	2D
TPV205	3D	SW	Homog.	Two patches, strike-slip	Vertical plane	Elastic	TPV5
TPV210	3D	SW	Homog.	depth-dep., dip-slip	Dipping plane	Elastic	TPV10

*SW, slip-weakening fault friction; RS-AL, rate–state fault friction with an ageing law; RS-SL-SRW, rate–state fault friction with a slip law with strong rate weakening; TP-RS-SRW, thermal pressurization with rate–state fault friction using a slip law with strong rate weakening.
†Rock structure includes material velocities and densities; homog., homogeneous.
‡Initial stress outside the nucleation zone; depth-dep., depth-dependent; heterog., heterogeneous; prop. to shear mod., proportional to shear modulus.
§ExGM, extreme ground motion.

the geometrical situation of the Shoreline and Hosgri faults near Diablo Canyon Nuclear Power Plant on the Central Coast in California (Hardebeck, 2013), a motivating factor for creating this benchmark. The main fault is continuous and can have non-zero slip at the junction where the two faults meet. The branch fault is constrained to have zero slip at the junction, so the two faults are not directly connected and a rupture must jump a short distance to transition from one fault to the other. This short distance (a small gap between the faults) is an artifact, which is needed to construct a computer implementation of the branch in many numerical techniques. The rupture nucleates at mid-depth on the vertical rectangular main fault, in a location that is not near the branch, then spontaneously propagates along the main fault both toward and away from the branch, up to the Earth's surface, and down to the bottom of the main fault. TPV14 and TPV15 are provided in both 2D and 3D versions. When the codes were used to simulate these two benchmarks, the results roughly matched but we wanted to understand the branch fault case better, so later we used this same basic idea about the fault geometry and designed additional benchmarks with different initial conditions.

TPV16 and TPV17

These two exercises return to the case of a single vertical strike-slip fault that intersects the Earth's surface. The primary new feature is the randomly generated heterogeneous initial stresses on the fault surface (Fig. 7). Heterogeneous initial stresses have been implemented in earthquake simulations over the years (e.g., Mikumo and Miyatake, 1978; Oglesby and Day, 2002; Ripperger *et al.*, 2007; Andrews and Ma, 2016) to produce more realistic variability in both the on-fault rupture behavior and the simulated ground shaking. The earthquake rupture is artificially nucleated using a new two-step method; the first stage is a circular zone of forced rupture, and the second stage is a larger circular zone of reduced fracture energy. The hypocenter is placed at a location where the random initial stress

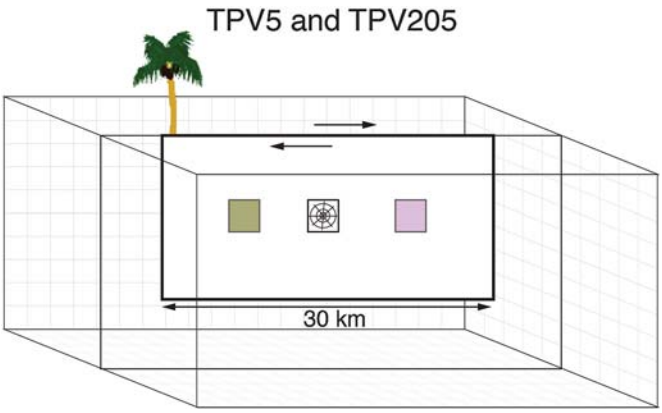

▲ **Figure 4.** TPV5: The earthquake rupture is artificially nucleated in a square zone at the center of the fault surface. The rupture then spontaneously propagates over the rest of the fault surface. As it propagates away from the nucleation zone, it encounters two square patches with initial stress conditions that are different from the rest of the fault surface. TPV205 is the same as TPV5; TPV205 is a convergence test with respect to grid size.

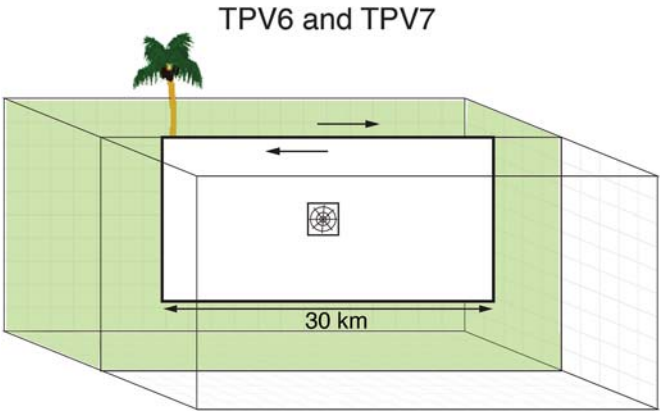

▲ **Figure 5.** TPV6 and TPV7: The earthquake rupture is artificially nucleated in a square zone at the center of the fault surface. The rupture then spontaneously propagates over the rest of the fault surface. The fault surface is the boundary between rocks with different elastic moduli. This material contrast is stronger for TPV6 than it is for TPV7.

happens to be high. The rupture then spontaneously propagates to the left, right, and bottom edges of the fault where it is stopped by strong fault regions, and ruptures up to the Earth's surface. TPV16 and TPV17 are the same except that they have different randomly generated initial stress patterns.

TPV18, TPV19, TPV20, and TPV21

These four exercises return to the case of a branching fault and use the same fault geometry as TPV14 and TPV15. TPV18 and TPV19 are right-lateral vertical strike-slip faults, and TPV20 and TPV21 are left-lateral vertical strike-slip faults. All four have right branches. TPV18 and TPV20 assume linear elastic

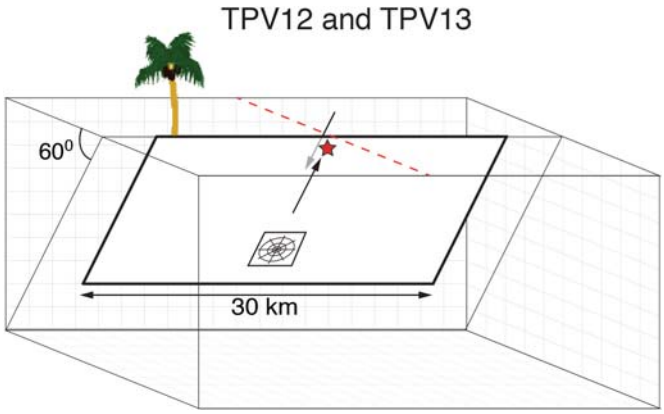

▲ **Figure 6.** TPV12 and TPV13: The earthquake rupture is artificially nucleated in a square zone near the bottom of the dipping fault surface. The rupture then spontaneously propagates very quickly over the rest of the fault surface and produces extreme ground shaking, including at the station of interest (red star) that is 300 m deep and 1 km away from the fault. Dashed red line shows where the 2D versions of these two benchmarks intersect the Earth's surface. The surrounding rocks respond elastically in TPV12 and plastically in TPV13.

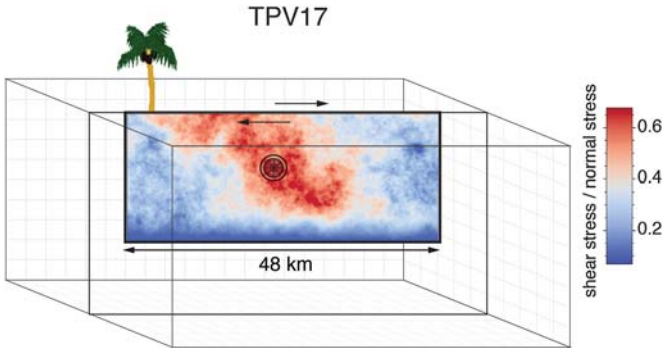

▲ **Figure 7.** TPV17: The earthquake rupture is artificially nucleated in a circular zone on the fault surface. The rupture then spontaneously propagates outward on the fault surface and encounters heterogeneous stochastic initial stress conditions, some of which prevent it from propagating into certain regions on the fault surface. Colors indicate the ratio of shear stress to normal stress at locations on the fault surface, at the beginning of the simulation. As the earthquake rupture propagates on the fault surface, these stress values (and stress ratios) change with time. These time-dependent stress changes occur for all of the dynamic rupture simulations described in this article and are a feature of dynamic rupture simulations in general. Exercise TPV16 is similar to TPV17; it just uses a different pattern of stochastic initial stress.

rock properties (the same properties as in TPV12). TPV19 and TPV21 assume that the rock properties are nonassociative Drucker–Prager plasticity with yielding in shear (the same properties as in TPV13). The nucleation method is the same as that used in TPV16 and TPV17. The reuse of fault geom-

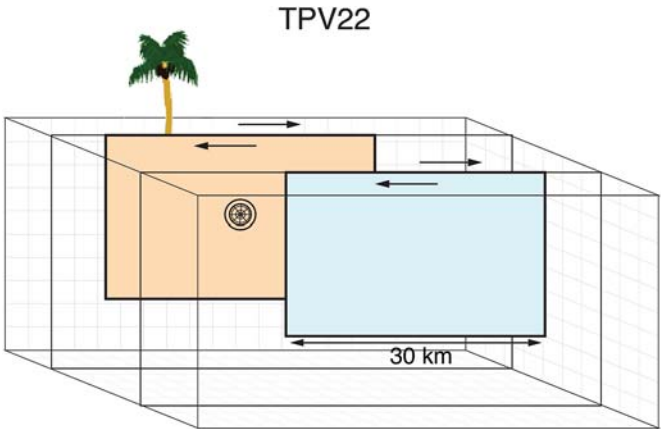

▲ **Figure 8.** TPV22: The earthquake rupture is artificially nucleated in a circular zone in the center of the first fault surface. The rupture then spontaneously propagates on the first fault, and jumps to rupture a second parallel fault surface.

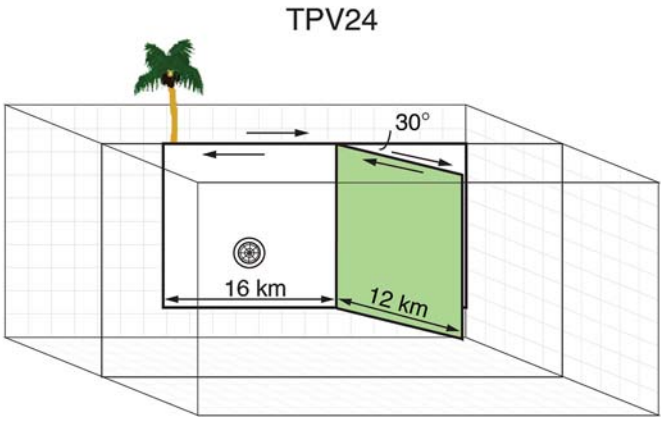

▲ **Figure 9.** TPV24: The earthquake rupture is artificially nucleated in a circular zone on the main fault surface. The rupture then spontaneously propagates on the main fault and encounters a branch (green rectangle) in the fault geometry. The closest edge of the branch fault surface ends at the main fault, at a vertical junction line, and slip on the branch fault surface is constrained to be zero at this location. For TPV24, a releasing branch, the main fault surface and the branch fault surface both rupture in their entirety. This releasing branch fault geometry was also used for TPV14, TPV18, and TPV19.

etry, material properties, and nucleation method from earlier exercises is one way that we proceed incrementally in designing new exercises. These exercises include gravity, hydrostatic fluid pressure (which remains constant during the simulation), and a depth-dependent initial stress tensor that is specified throughout the model volume. As with TPV14 and TPV15, the branch fault and the main fault are not directly connected.

TPV22 and TPV23

These two exercises examine the case of a stepover between parallel vertical right-lateral strike-slip faults (e.g., Kase and Kuge, 2001; Harris *et al.*, 2002). Our group hypothesized that these fault-geometry benchmarks, which are simpler than the branched fault case would be an easier test of the codes, and this was indeed the situation, with qualitatively good matches occurring among the code results. TPV22 (Fig. 8) is a right step between the right-lateral strike-slip faults, a dilational step. TPV23 is a left step between the right-lateral strike-slip faults, a compressional step. The nucleation process is varied from previous benchmarks in that it is accomplished using a smoothed forced rupture, with a forced rupture velocity that decreases with distance from the hypocenter, so as to create a gradual transition from forced rupture to spontaneous rupture. The description of the fault boundary condition has been changed so that a node that lies precisely on the border of a fault is not permitted to slip; this makes the fault size less dependent on the mesh discretization size. In addition, in contrast to previous benchmarks, the rupture is gradually stopped at the bottom of the fault by gradually tapering the initial shear stress to a low value.

TPV24 and TPV25

These two exercises are one final visit to the fault branch geometry, using the same fault geometry as TPV14–TPV15 and TPV18–TPV21. Both benchmarks assume vertical strike-slip faults. TPV24 (Fig. 9) is a right-lateral strike-slip fault with a branch to the right (releasing branch), TPV25 is a left-lateral strike-slip fault with a branch to the right (restraining branch). The nucleation location has been changed, and the nucleation method is the technique first introduced in TPV22–TPV23. Although the models are elastic, they are set up appropriately for inelastic models and include gravity, fluid pressure, and an initial stress tensor.

TPV26 and TPV27

These two exercises are a test of using rock properties that are viscoplastic. The rock response in TPV26 is linear elastic, in TPV27 it is nonassociative Drucker–Prager viscoplasticity with yielding in shear. Viscoplasticity may be implemented in either a kinematic (e.g., Roten *et al.*, 2014) or dynamic earthquake rupture simulation (e.g., Ma and Andrews, 2010; Shi and Day, 2013; Wollherr and Gabriel, 2016; Roten *et al.*, 2017) to prevent the buildup of unrealistically high stress in the rocks surrounding an earthquake rupture. The advantage of viscoplasticity is that it regularizes the calculation, as opposed to a plastic model that might fail to converge or have nonunique solutions (Andrews, 2005; Templeton and Rice, 2008). Both the TPV26 and TPV27 exercises are a single vertical strike-slip rectangular fault set in a homogeneous velocity and density structure. Nucleation uses the same method as in TPV22–TPV25. Gravity and fluid pressure are included. Both benchmarks use slip-weakening fault friction.

TPV28

This exercise is an initial foray into fault roughness. Although stochastic initial stress conditions such as those in TPV16–17 have become more common over the decades, geometrical fault roughness (e.g., Shi and Day, 2013; Duru and Dunham, 2016;

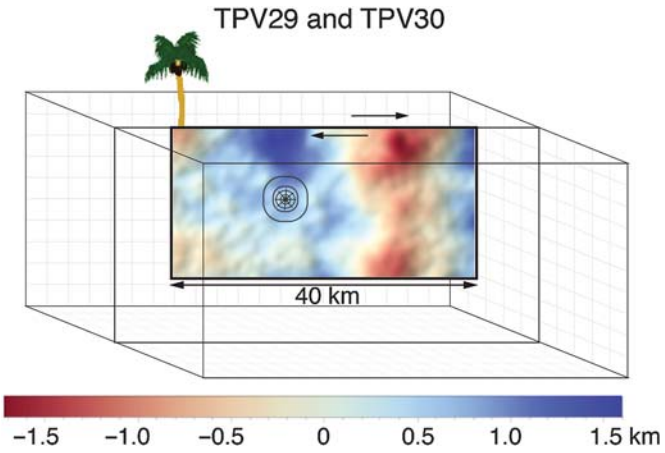

▲ **Figure 10.** TPV29 and TPV30: The earthquake rupture is artificially nucleated in a circular zone on the fault surface. The rupture then spontaneously propagates where it is able to, on the fault surface which has 3D stochastic geometrical roughness (blue and red colors). In TPV29, the surrounding rocks respond elastically, in TPV30 the surrounding rocks respond viscoplastically. Colors show the height of the roughness relative to a flat plane.

Mai *et al.*, 2017; Ulrich and Gabriel, 2017) is more challenging to implement, particularly for certain types of codes. In this benchmark, two geometrical protuberances are set on the fault surface of an otherwise vertical strike-slip fault. The initial shear and normal stresses on the fault are obtained by resolving a uniform regional stress tensor onto the fault. Nucleation is achieved by applying an additional initial shear stress in a circular nucleation patch, which gradually tapers off at the edge of the patch.

TPV29 and TPV30

These two exercises continue our exploration of geometrical fault roughness and implement stochastic fault roughness. The strike-slip fault is a vertical fault surface before the geometrical roughness is added. TPV29 is elastic and TPV30 is viscoplastic (Fig. 10). The shear and normal stresses on the rough fault surface are obtained by resolving a depth-dependent regional stress tensor onto the rough fault surface. Gravity and a constant fluid pressure are included, with the fluid pressure hydrostatic. Nucleation uses the same method as in TPV22–TPV27.

TPV31, TPV32, TPV33, and TPV34

These four exercises examine how well codes implement heterogeneous velocity structures. All are vertical strike-slip rectangular faults. TPV31 and TPV32 have 1D velocity structures, in which the velocity increases with depth. The TPV31 velocity structure has several discontinuities, whereas in TPV32 it is continuous. TPV33 has a 1D velocity structure that varies perpendicular to the fault, creating a low-velocity zone surrounding the fault surface. TPV34 has a 3D velocity structure resembling the deeper structure in the Imperial Valley, California, region. The initial stresses in TPV31, TPV32, and TPV34 are proportional to the shear modulus, to approximate constant-strain conditions. In TPV33, the initial shear stress is tapered on all four sides of the fault surface, so that the rupture stops spontaneously before reaching any fault edge. All four exercises use the TPV28 nucleation method, and all assume that the rocks respond elastically and fault friction is slip weakening.

TPV35

This exercise reproduces a spontaneous rupture simulation by Ma *et al.* (2008) of the 2004 magnitude 6.0 Parkfield, California, earthquake (Fig. 11, also see Figs. 2 and 3). The 3D velocity structure consists of two 1D vertical structures that abut at the planar vertical right-lateral strike-slip fault. The initial stress conditions and friction parameters on the fault surface are heterogeneous. The rock responds elastically, fault friction is slip weakening, and the seismic stations are located at the same locations on the Earth's surface as a set of strong ground motion stations that recorded the 2004 magnitude 6.0 Parkfield, California, earthquake. This benchmark provides a glimpse of the challenges involved with code validation, especially if the goal was to validate against recorded strong ground motion time-series data, which are also provided in the benchmark exercise. On the other hand, the codes themselves produced results that matched each other well for many of the seismic stations, and demonstrate that this is a useful exercise for code verification.

TPV101 and TPV102

The five exercises TPV101–TPV105 examine the use of fault friction other than slip weakening. All five exercises assume that the rock response is elastic. TPV101 and TPV102 (Fig. 12) explore the use of rate–state friction using an ageing law (e.g., Rice *et al.*, 2001). TPV101 is a homogeneous full-space; TPV102 is a homogeneous half-space. The fault is a planar rectangular vertical strike-slip fault. The main part of the rectangular fault that is intended to rupture has velocity-weakening friction. Surrounding this is another region of finite width on the fault surface where the fault friction smoothly transitions from velocity-weakening friction to velocity-strengthening friction. Then outside of this transition zone, the rest of the fault surface is velocity-strengthening friction. The rupture propagates through the transition zone into the velocity-strengthening region, where it smoothly and spontaneously arrests. Nucleation is done by imposing additional shear stress in a circular patch surrounding the hypocenter. Unlike our slip-weakening benchmarks, the nucleation stress is not imposed instantaneously at the start of the simulation, but instead increases smoothly from zero to its full value over a finite time interval.

TPV103 and TPV104

These two exercises explore the use of rate–state friction using a slip law with strong rate weakening (e.g., Rice, 2006; Beeler *et al.*, 2008; Goldsby and Tullis, 2011). TPV103 is a homogeneous full-space; TPV104 (Fig. 12) is a homogeneous half-space. The fault is a planar rectangular vertical strike-slip fault. Similar to TPV101 and TPV102, the main rupture region has velocity-weakening friction, a zone on the fault surface with

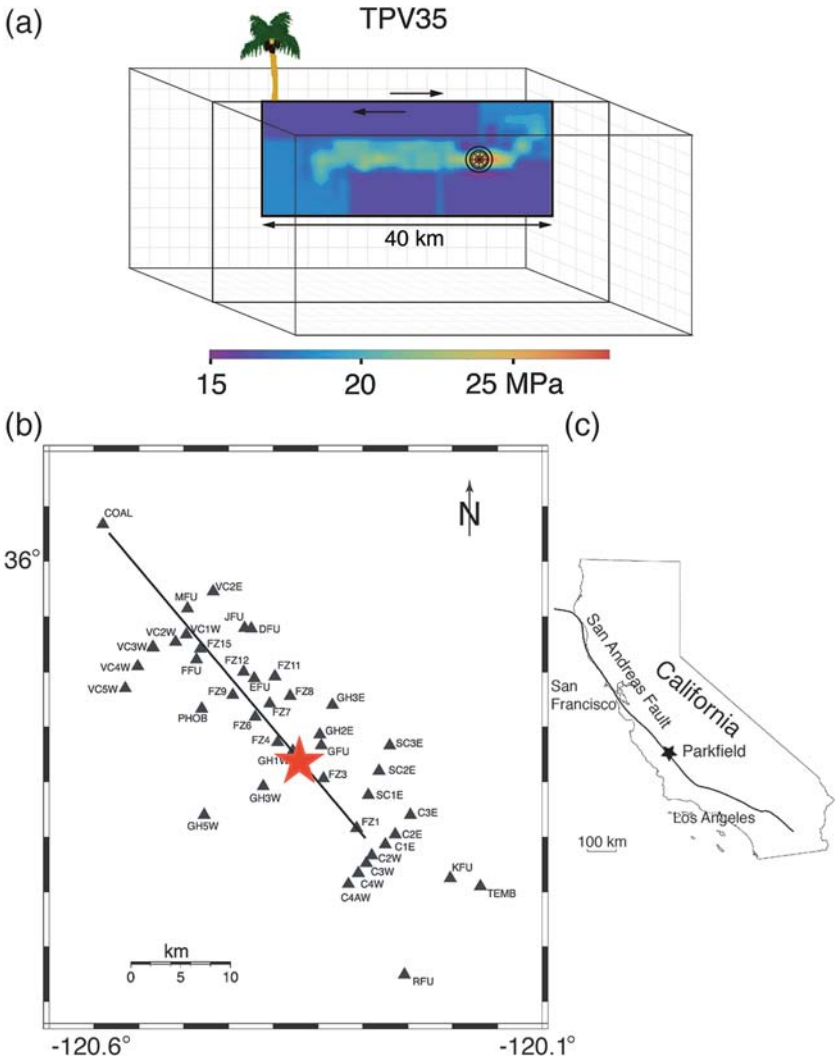

▲ **Figure 11.** TPV35: (a) The earthquake rupture is artificially nucleated in a circular zone on the vertical planar fault surface that has the depicted initial shear stress pattern. The rupture then spontaneously propagates on the fault surface, before eventually stopping. TPV35 uses the Ma *et al.* (2008)-favored spontaneous rupture model of the 2004 magnitude 6.0 Parkfield, California, earthquake. This exercise investigates the rupture pattern on the fault surface itself, as well as the simulated ground shaking at (b) seismic stations on the Earth's surface (triangles) in the region near Parkfield, for comparison with real seismograms recorded at these seismic stations during the 2004 Parkfield earthquake. (b) Modified from figure 10 of Ma *et al.* (2008) and (c) modified from figure 1 of Simpson *et al.* (2006). The stars in (b) and (c) show the location of the epicenter.

transitional friction surrounds the main fault rupture region, and the outer regions on the fault surface have velocity-strengthening friction. The nucleation method is the same as in TPV101 and TPV102.

TPV105

This exercise is a 2D benchmark that explores the use of thermal pressurization, with rate–state fault friction and a slip law that assumes strong rate weakening (e.g., Sibson, 1973; Andrews, 2002; Rice, 2006). The fault is a vertical strike-slip fault. TPV105 exists only as a 2D benchmark because we were unable to find a successful set of parameters for a 3D version.

RESULTS FOR TWO OF OUR BENCHMARK EXERCISES, TPV16 AND TPV25

Our group has produced results for all of our benchmark exercises. Because of space constraints in this article, we show results for just two of them. TPV16 (Fig. 13) is the first of our two exercises with stochastic initial stresses (the second TPV17 is shown in Fig. 7). Twelve codes participated in the TPV16 exercise. These codes produced results that matched each other well, as demonstrated by the agreements among plots of the rupture progress on the fault surface and the agreement, up to at least 3 Hz, among the synthetic seismograms at the Earth's surface (Fig. 13).

TPV24 and TPV25 are our final attempts at the fault-branch exercises. The location of the junction between the main fault and the branch fault is important, as we learned from our earlier fault branch exercises. For TPV24 and TPV25, we defined the end of the branch that is closest to the main fault so that its location is not dependent on the discretization size used in the computational mesh. As in our previous branch fault benchmarks, the main fault is continuous while the branch fault ends at the junction and is effectively disconnected from the main fault. We had success matching the code results, including rupture progress and synthetic seismograms up to at least 3 Hz, for both TPV24 and TPV25, when the simulations assumed the same conditions at the fault junction. TPV25 results are shown in Figure 14. Most of the simulations did not allow the rupture to slip at the junction between the main and branch faults, effectively forcing the rupture to jump between the two faults, however two of the simulations did allow the connection to occur. Although the nature of the fault junction did not have a significant impact on the main fault's rupture propagation pattern, it did affect both the ability of the branching fault to fully rupture and the seismograms at the station near the fault junction, as shown in Figure 14.

DISCUSSION AND CONCLUSIONS

Dynamic (spontaneous) earthquake rupture simulations are used to understand the mechanics of specific earthquakes that have already occurred, and to envision the behavior of earthquakes in the future. There are, however, no known analytic

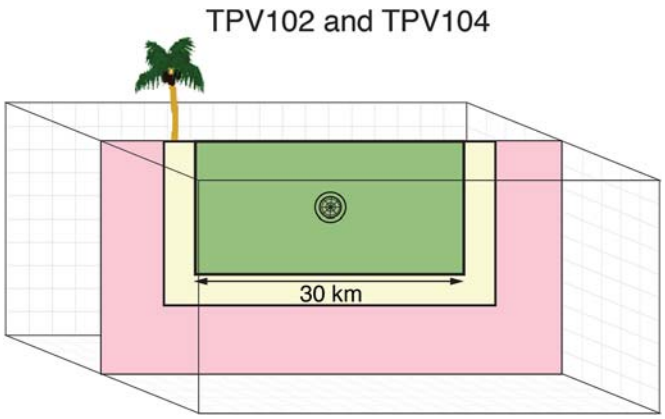

▲ **Figure 12.** TPV102 and TPV104: The earthquake ruptures a region of the vertical planar fault that has velocity-weakening friction (green). When the rupture reaches the side and bottom edges of this velocity-weakening region, it encounters a finite-width transitional region (yellow) where the friction smoothly changes from velocity weakening (green) on the inside to velocity strengthening (red) on the outside. This change in the fault friction acts to stop the rupture from propagating farther along or deeper on the fault surface.

solutions with which these complex physics-based codes can be tested; so, it is difficult to know if conclusions drawn from using one or two spontaneous rupture codes in isolation are reliable. This issue motivated us to develop code verification tests to check if the codes are working as intended. Our group's code-verification exercises implement a range of features used in spontaneous earthquake rupture simulations, and many of the benchmarks were designed to investigate scientific problems at the forefront in the earthquake physics and ground-motion communities. These include benchmark exercises of large (e.g., magnitude 7) earthquake settings with variable fault geometry, with variable initial stress conditions, with variable rock properties, and with variable friction (Table 2). We use these benchmark exercises to perform comparisons of the results produced by multiple codes, intercode comparisons. Our comparisons to date have primarily focused on comparing on-fault earthquake rupture patterns and synthetic seismograms both at the Earth's surface and at depth, but on occasion we also studied time-dependent stresses and other features.

Our most satisfying code verification exercises have been those for which there was a clear agreement among the code results for rupture-front patterns and for on and off-fault seismograms, as observed using both qualitative judgment and quantitative metrics (Barall and Harris, 2015). Our successful sets of code comparison results in more recent years (those constructed after the exercises presented in our earlier papers, Harris *et al.*, 2009, 2011) include the heterogeneous initial stress conditions exercises (TPV16 and TPV17), and at least three of the exercises that test how well the codes handle fault geometry: the fault stepover (TPV22 and TPV23), rough-fault elastic (TPV29), and fault branch (TPV24 and TPV25) exercises. Checking the ability of the codes to handle different types of off-fault rock response, the planar fault elastic and viscoplastic benchmarks (TPV26 and TPV27) produced good matches among the codes' results. The group also had success with the velocity structure benchmarks for the seismic stations that were not very far (less than 15 km) from the fault.

More distant seismic stations challenged the codes' capabilities to produce matching synthetic seismograms for times that were many seconds after the first seismic wave arrivals. In some cases, this was due to computational limits that restricted the sizes of the model meshes. This limitation allowed spurious waves that reflected from the side and bottom boundaries of the too-small model meshes to corrupt the seismic signals at stations far from the faults. Another possible factor is that numerical dispersion of the wave propagation and approximation errors in modeling the rupture process tend to accumulate over time, so that in lengthy simulations needed to produce seismograms at distant stations, the code results tend to gradually diverge from each other.

Overall, the benchmark exercises for which the codes' results have had the least agreement are the earlier (those before TPV24 and 25) benchmarks that investigate the case of a fault branch. In the fault branch rupture simulations, the dynamic rupture is very sensitive to the nature of the junction between the main fault and the branch fault, resulting in different outcomes among the codes for the rupture extent, depending on how far apart the two faults are at the junction. In our more recent years, we explored changes in our method for artificial rupture nucleation, better definitions of the borders of the fault surface so that they are less dependent on the grid size used in the models, and the inclusion of cohesion for the portions of the fault surface that are near the Earth's surface, all of which have improved the results for code verification. These are also useful lessons for spontaneous rupture simulations in general.

In Table 2, we list the suite of benchmark exercises and note a few that we consider from our earlier years as classics. Higher number benchmarks (aside from some of the fault branch benchmarks) that implement slip-weakening fault friction also satisfy this criterion. The rate–state friction benchmarks (TPV101–TPV105) have also held up well over the years and are worthwhile code verification tests for new or newly revised codes.

The suite of exercises that we described in this article is a means for testing the repeatability and reliability of spontaneous rupture codes, that is, if they are computing what the code developers have intended. The next step following our code verification exercises will be code validation. Code validation has been conducted by groups investigating other earthquake science questions, including the SCEC Geodetic Transient-detection validation group (Lohman and Murray, 2013), the Source Inversion Validation exercise (Mai *et al.*, 2016), and the SCEC Broadband Platform validation exercise (Goulet *et al.*, 2014). With code validation, scientists start with the knowledge that their codes are working as intended, then confidently move forward to concentrate on understanding how and why their simulations agree or disagree with the data produced by real earthquakes. The dynamic rupture code validation enterprise will not be easy given Earth's complexity, but

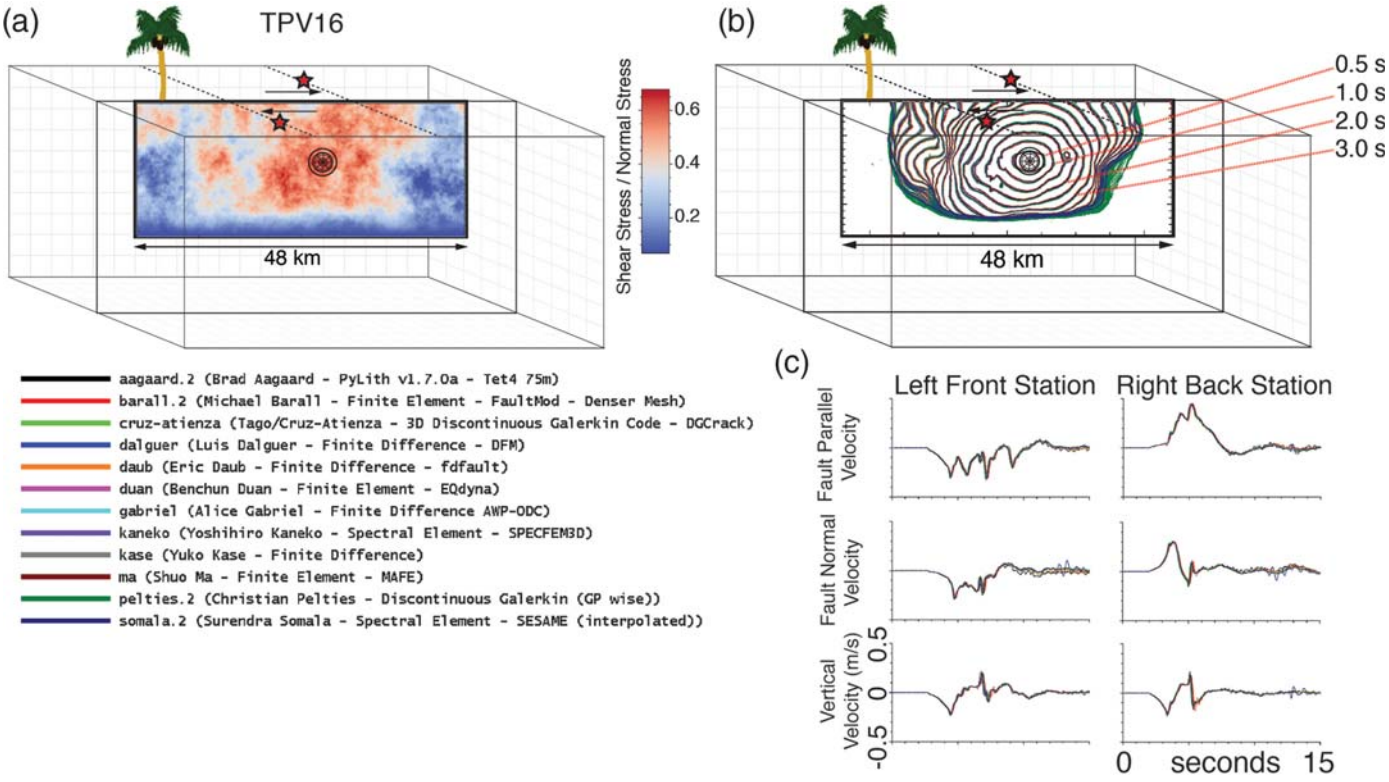

▲ **Figure 13.** Results from 12 codes used to perform TPV16. (a) TPV16 assumes stochastic initial stress conditions on the fault surface, depicted as the ratio of initial shear stress to initial normal stress. The circled area shows the nucleation zone on the fault surface. Red stars show 2 of the 16 off-fault stations where synthetic seismograms are produced for this exercise. These two stations are located on the Earth's surface, 9 km along strike from the fault center and 6 km perpendicular distance from the fault, with the left-front station at (−9 km, −6 km) and the right-back station at (+9 km, +6 km). (b) The earthquake rupture nucleates starting at 0 s. The contours show the subsequent progress of the rupture front on the fault surface, as a function of time, in 0.5 s intervals, as it propagates away from the nucleation zone. Each code's result is shown with its own color, so there are 12 sets of contours. (c) Synthetic seismograms filtered at 3 Hz (using an acausal two-poles two-passes low-pass Butterworth filter), produced by each of the 12 codes (same codes/colors as b) at the two off-fault stations. Horizontal fault-parallel, horizontal fault-normal, and vertical velocities.

our code verification exercises will have provided the essential first steps toward success.

DATA AND RESOURCES

The benchmark exercise TPV35 includes the option to compare simulations with data from the 2004 Parkfield earthquake, and these data came from a published source listed in the References. The other benchmark exercises described in this particle are purely computational simulations. The article refers to the Southern California Earthquake Center-U.S. Geological Survey (SCEC-USGS) dynamic rupture code verification website (scecdata.usc.edu/cvws, last accessed March 2018). This website contains the descriptions for all of the benchmark exercises, in addition to other information about the project. Many of our group's dynamic earthquake rupture codes are listed in Table 1. Codes that can be accessed online include fdfault (https://github.com/egdaub/fdfault), PyLith (https://geodynamics.org/cig/software/pylith/), SeisSol (https://github.com/SeisSol/SeisSol/wiki), SPECFEM3D (https://geodynamics.org/cig/software/specfem3d/), and WaveQLab3D (https://bitbucket.org/ericmdunham/waveqlab3d). All websites were last accessed on March 2018.

ACKNOWLEDGMENTS

This article received insightful U.S. Geological Survey (USGS) internal reviews from Andy Barbour and Fred Pollitz, and helpful journal reviews from *SRL* Editor-in-Chief Zhigang Peng, an anonymous *SRL* Associate Editor, and from *SRL* reviewers Martin Mai and an anonymous reviewer. Funding for this Southern California Earthquake Center (SCEC)-USGS project was provided by SCEC, by the USGS, and by Pacific Gas and Electric Company (via SCEC and via the USGS-PGE CRADA). We authors are appreciative of contributions from students, postdocs, and junior and senior researchers who have helped and encouraged us over the years on our path forward. These include but are not limited to Ralph Archuleta, Steve Day, Nadia Lapusta, Joe Andrews, Geoff Ely, Percy Galvez, Elizabeth

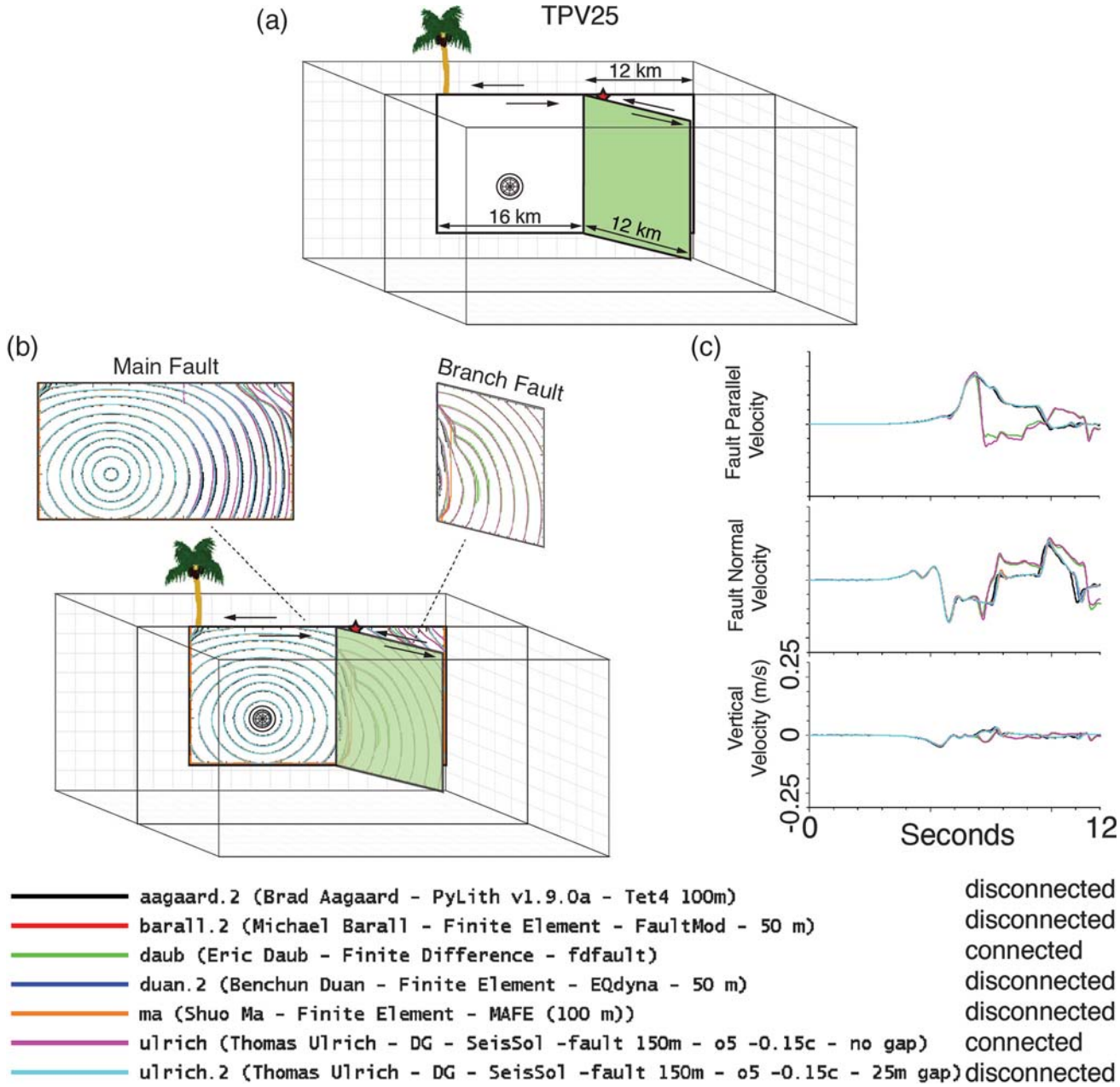

▲ **Figure 14.** Results from six codes used to produce seven simulations (each shown in its own color) of TPV25. (a) TPV25 has a 30° right branch in a left-lateral vertical strike-slip fault (restraining branch). The circled area is the nucleation zone. The red star is an off-fault station on the Earth's surface near the intersection of the main fault and branch fault, one of the locations where synthetic seismograms are produced for this exercise. Five of the seven simulations used the codes PyLith, FaultMod, EQdyna, MAFE, and SeisSol (25 m gap), shown in black, red, dark blue, orange, and light blue, respectively, produced results assuming the branch fault is disconnected from the main fault. Two of the seven simulations, using the codes fdfault and SeisSol (no gap), shown in green and pink, respectively, produced results assuming the branch fault is connected to the main fault. (b) Progress of the rupture front on the fault surface, as a function of time, produced by each of the seven simulations, contoured at 0.5 s intervals. Contours show when and where each simulation propagates away from the nucleation zone on the main fault, then onto the branch fault. The rupture successfully propagates over the entire main fault for all seven simulations, but the rupture barely propagates on the branch fault for the five simulations that assume the two faults are disconnected. In contrast, the rupture is able to fully propagate on the branch fault for the simulations that assume the branch fault is connected to the main fault (two codes' results shown in pink and green). (c) The seven simulations, each using the same color scheme as in (b), produce synthetic seismograms at the off-fault station. Horizontal fault-parallel, horizontal fault-normal, and vertical velocities, all filtered at 3 Hz (using an acausal two-poles two-passes low-pass Butterworth filter). The seismograms are affected by whether or not the branch fault is assumed to be connected to the main fault, as demonstrated by the well-matched green and pink seismograms (connected-fault simulations), which differ from the other five well-matched seismograms (disconnected-fault simulations).

Templeton-Barrett, Seok Goo Song, David Oglesby, Yi Liu, Arben Pitarka, Nora DeDontney, Hiro Noda, Ryan Payne, Harsha Bhat, Ahmed Elbanna, Xiao Ma, Peter Moczo, Martin Mai, Jim Rice, Renata Dmowska, Tom Hanks, Paul Somerville, and Norm Abrahamson. This is SCEC Publication Number 7960.

Any use of trade, firm, or product names is for descriptive purposes only and does not imply endorsement by the U.S. Government.

REFERENCES

Aagaard, B. T., T. H. Heaton, and J. F. Hall (2001). Dynamic earthquake ruptures in the presence of lithostatic normal stresses: Implications for friction models and heat production, *Bull. Seismol. Soc. Am.* **91,** no. 6, 1765–1796, doi: 10.1785/0120000257.

Aagaard, B. T., M. G. Knepley, and C. A. Williams (2013). A domain decomposition approach to implementing fault slip in finite-element models of quasi-static and dynamic crustal deformation, *J. Geophys. Res.* **118,** 3059–3079, doi: 10.1002/jgrb.50217.

Andrews, D. J. (1976). Rupture propagation with finite stress in antiplane strain, *J. Geophys. Res.* **81,** no. 20, 3575–3582.

Andrews, D. J. (2002). A fault constitutive relation accounting for thermal pressurization of pore fluid, *J. Geophys. Res.* **107,** no. B12, 2363, doi: 10.1029/2002JB001942.

Andrews, D. J. (2004). Rupture models with dynamically determined breakdown displacement, *Bull. Seismol. Soc. Am.* **94,** no. 3, 769–775, doi: 10.1785/0120030142.

Andrews, D. J. (2005). Rupture dynamics with energy loss outside the slip zone, *J. Geophys. Res.* **110,** no. B01307, doi: 10.1029/2004JB003191.

Andrews, D. J., and S. Ma (2016). Validating a dynamic earthquake model to produce realistic ground motion, *Bull. Seismol. Soc. Am.* **106,** no. 2, 665–672, doi: 10.1785/0120150251.

Andrews, D. J., T. C. Hanks, and J. W. Whitney (2007). Physical limits on ground motion at Yucca Mountain, *Bull. Seismol. Soc. Am.* **97,** no. 6, 1771–1792, doi: 10.1785/0120070014.

Barall, M. (2009). A grid-doubling finite-element technique for calculating dynamic three-dimensional spontaneous rupture on an earthquake fault, *Geophys. J. Int.* **178,** no. 2, 845–859, doi: 10.1111/j.1365-246X.2009.04190.x.

Barall, M., and R. A. Harris (2015). Metrics for comparing dynamic earthquake rupture simulations, *Seismol. Res. Lett.* **86,** no. 1, 223–235, doi: 10.1785/0220140122.

Beeler, N. M., T. E. Tullis, and D. L. Goldsby (2008). Constitutive relationships and physical basis of fault strength due to flash heating, *J. Geophys. Res.* **113,** no. B01401, doi: 10.1029/2007JB004988.

Bizzarri, A. (2010). How to promote earthquake ruptures: Different nucleation strategies in a dynamic model with slip-weakening friction, *Bull. Seismol. Soc. Am.* **100,** no. 3, 923–940, doi: 10.1785/0120090179.

Dalguer, L. A., and S. M. Day (2007). Staggered-grid split-node method for spontaneous rupture simulation, *J. Geophys. Res.* **112,** no. B02302, doi: 10.1029/2006JB004467.

Daub, E. G. (2016). Meet a new code: Daub finite difference, Presentation at the *March 2016 SCEC Rupture Dynamics Code Validation Workshop*, http://scecdata.usc.edu/cvws/download/mar11_2016/Daub_cvws_0311.pdf (last accessed March 2018).

Day, S. M. (1982). Three-dimensional simulation of spontaneous rupture: The effect of nonuniform prestress, *Bull. Seismol. Soc. Am.* **72,** no. 6, 1881–1902.

Day, S. M., and G. P. Ely (2002). Effect of a shallow weak zone on fault rupture: Numerical simulation of scale-model experiments, *Bull Seismol. Soc. Am.* **92,** 3006–3021.

Day, S. M., L. A. Dalguer, N. Lapusta, and Y. Liu (2005). Comparison of finite difference and boundary integral solutions to three-dimensional spontaneous rupture. *J. Geophys. Res.* **110,** no. B12307, doi: 10.1029/2005JB003813.

Duan, B., and D. D. Oglesby (2006). Heterogeneous fault stresses from previous earthquakes and the effect on dynamics of parallel strike-slip faults, *J. Geophys. Res.* **111,** no. B05309, doi: 10.1029/2005JB004138.

Duru, K., and E. M. Dunham (2016). Dynamic earthquake rupture simulations on nonplanar faults embedded in 3D geometrically complex, heterogeneous elastic solids, *J. Comput. Phys.* **305,** 185–207.

Ely, G. P., S. M. Day, and J.-B. Minster (2009). A support-operator method for 3-D rupture dynamics, *Geophys. J. Int.* **177,** 1140–1150, doi: 10.1111/j.1365-246X.2009.04117.x.

Galis, M., C. Pelties, J. Kristek, P. Moczo, J.-P. Ampuero, and P. M. Mai (2015). On the initiation of sustained slip-weakening ruptures by localized stresses, *Geophys. J. Int.* **200,** 890–909, doi: 10.1093/gji/ggu436.

Galvez, P., J. P. Ampuero, L. A. Dalguer, S. N. Somala, and T. F. Nissen-Meyer (2014). Dynamic earthquake rupture modelled with an unstructured 3-D spectral element method applied to the 2011 M 9 Tohoku earthquake, *Geophys. J. Int.* **198,** no. 2, 1222–1240, doi: 10.1093/gji/ggu203.

Goldsby, D., and T. E. Tullis (2011). Flash heating leads to low frictional strength of crustal rocks at earthquake slip rates, *Science* **334,** no. 6053, 216–218, doi: 10.1126/science.1207902.

Goulet, C. A., N. A. Abrahamson, P. G. Somerville, and K. E. Wooddell (2014). The SCEC broadband platform validation exercise: Methodology for code validation in the context of seismic-hazard analyses, *Seismol. Res. Lett.* **86,** no. 1, 17–26, doi: 10.1785/0220140104.

Hardebeck, J. L. (2013). Geometry and earthquake potential of the Shoreline fault, central California, *Bull. Seismol. Soc. Am.* **103,** no. 1, 447–462, doi: 10.1785/0120120175.

Harris, R. A. (2004). Numerical simulations of large earthquakes: Dynamic rupture propagation on heterogeneous faults, *Pure Appl. Geophys.* **161,** nos. 11/12, 2171–2181, doi: 10.1007/s00024-004-2556-8.

Harris, R. A., and R. J. Archuleta (2004). Earthquake rupture dynamics: Comparing the numerical simulation methods, *Eos Trans. AGU* **85,** no. 34, 321–321, doi: 10.1029/2004EO340003.

Harris, R. A., M. Barall, D. J. Andrews, B. Duan, E. M. Dunham, S. Ma, A.-A. Gabriel, Y. Kaneko, Y. Kase, B. Aagaard, et al. (2011). Verifying a computational method for predicting extreme ground motion, *Seismol. Res. Lett.* **82,** no. 5, 638–644, doi: 10.1785/gssrl.82.5.638.

Harris, R. A., M. Barall, R. Archuleta, E. Dunham, B. Aagaard, J. P. Ampuero, H. Bhat, V. Cruz-Atienza, L. Dalguer, P. Dawson, et al. (2009). The SCEC/USGS dynamic earthquake rupture code verification exercise, *Seismol. Res. Lett.* **80,** no. 1, 119–126, doi: 10.1785/gssrl.80.1.119.

Harris, R. A., J. F. Dolan, R. Hartleb, and S. M. Day (2002). The 1999 İzmit, Turkey, earthquake: A 3D dynamic stress transfer model of intraearthquake triggering, *Bull. Seismol. Soc. Am.* **92,** no. 1, 245–255, doi: 10.1785/0120000825.

Ida, Y. (1972). Cohesive force across the tip of a longitudinal-shear crack and Griffith's specific surface energy, *J. Geophys. Res.* **77,** no. 20, 3796–3805, doi: 10.1029/JB077i020p03796.

Kaneko, Y., N. Lapusta, and J. P. Ampuero (2008). Spectral element modeling of spontaneous earthquake rupture on rate and state faults: Effect of velocity-strengthening friction at shallow depths, *J. Geophys. Res.* **113,** no. B09317, doi: 10.1029/2007JB005553.

Kase, Y., and K. Kuge (2001). Rupture propagation beyond fault discontinuities: Significance of fault strike and location, *Geophys. J. Int.* **147,** no. 2, 330–342, doi: 10.1046/j.1365-246X.2001.00533.x.

Kozdon, J. E., L. C. Wilcox, and T. C. Warburton (2015). GPU-enabled rupture dynamics simulations, presented at the 2015 annual meeting of the Southern California Earthquake Center (Poster 246), *Proc. of the 2015 Annual Meeting of the Southern California Earthquake Center*, Palm Springs, California, Vol. XXV, p. 161.

Lohman, R. B., and J. R. Murray (2013). The SCEC geodetic transient-detection validation exercise, *Seismol. Res. Lett.* **84,** no. 3, 419–425, doi: 10.1785/0220130041.

Ma, S., and D. J. Andrews (2010). Inelastic off-fault response and three-dimensional dynamics of earthquake rupture on a strike-slip fault, *J. Geophys. Res.* **115,** no. B04304, doi: 10.1029/2009JB006382.

Ma, S., S. Custodio, R. J. Archuleta, and P. Liu (2008). Dynamic modeling of the 2004 M_w 6.0 Parkfield, California, earthquake, *J. Geophys. Res.* **113,** no. B02301, doi: 10.1029/2007JB005216.

Mai, P. M., M. Galis, K. K. S. Thingbaijam, J. C. Vyas, and E. M. Dunham (2017). Accounting for fault roughness in pseudo-dynamic ground-motion simulations, *Pure Appl. Geophys.* **174,** 3419–3450, doi: 10.1007/s00024-017-1536-8.

Mai, P. M., D. Schorlemmer, M. Page, J.-P. Ampuero, K. Asano, M. Causse, S. Custodio, W. Fan, G. Festa, M. Galis, et al. (2016). The earthquake-source inversion validation (SIV) project, *Seismol. Res. Lett.* **87,** no. 3, 690–708, doi: 10.1785/0220150231.

Mikumo, T., and T. Miyatake (1978). Dynamical rupture process on a three-dimensional fault with non-uniform frictions and near-field seismic waves, *Geophys. J. Roy. Astron. Soc.* **54,** 417–438.

Moczo, P., J. Kristek, M. Galis, P. Pazak, and M. Balazovjech (2007). The finite-difference and finite-element modeling of seismic wave propagation and earthquake motion, *Acta Phys. Slovaca* **57,** no. 2, 177–406.

Oglesby, D. D., and S. M. Day (2002). Stochastic fault stress: Implications for fault dynamics and ground motion, *Bull. Seismol. Soc. Am.* **92,** no. 8, 3006–3021, doi: 10.1785/0120010249.

Palmer, A. C., and J. R. Rice (1973). The growth of slip surfaces in the progressive failure of over-consolidated clay, *Proc. Math. Phys. Sci.* **332,** 527–548.

Pelties, C., J. de la Puente, J. P. Ampuero, G. Brietzke, and M. Käser (2012). Three-dimensional dynamic rupture simulation with a high-order Discontinuous Galerkin method on unstructured tetrahedral meshes, *J. Geophys. Res.* **117,** no. B02309, doi: 10.1029/2011JB008857.

Pelties, C., A. A. Gabriel, and J. P. Ampuero (2014). Verification of an ADER-DG method for complex dynamic rupture problems, *Geosci. Model Dev.* **7,** 847–866, doi: 10.5194/gmd-7-847-2014.

Ranjith, K., and J. R. Rice (2001). Slip dynamics at an interface between dissimilar materials, *J. Mech. Phys. Solid.* **49,** no. 2, 341–361.

Rice, J. R. (2006). Heating and weakening of faults during earthquake slip, *J. Geophys. Res.* **111,** no. B05311, doi: 10.1029/2005JB004006.

Rice, J. R., N. Lapusta, and K. Ranjith (2001). Rate and state dependent friction and the stability of sliding between elastically deformable solids, *J. Mech. Phys. Solid.* **49,** 1865–1898.

Ripperger, J., J. P. Ampuero, P. M. Mai, and D. Giardini (2007). Earthquake source characteristics from dynamic rupture with constrained stochastic fault stress, *J. Geophys. Res.* **112,** no. B04311, doi: 10.1029/2006JB004515.

Roten, D., Y. Cui, K. B. Olsen, S. M. Day, K. Withers, W. H. Savran, P. Wang, and D. Mu (2016). High-frequency nonlinear earthquake simulations on petascale heterogeneous supercomputers, *Proc. Supercomputing Conference*, Salt Lake City, Utah, November 2016.

Roten, D., K. B. Olsen, and S. M. Day (2017). Off-fault deformations and shallow slip deficit from dynamic rupture simulations with fault zone plasticity, *Geophys. Res. Lett.* **44,** 7733–7742, doi: 10.1002/2017GL074323.

Roten, D., K. B. Olsen, S. M. Day, Y. Cui, and D. Fah (2014). Expected seismic shaking in Los Angeles reduced by San Andreas fault zone plasticity, *Geophys. Res. Lett.* **41,** 2769–2777, doi: 10.1002/2014GL059411.

Shi, Z., and S. M. Day (2013). Rupture dynamics and ground motion from 3-D rough-fault simulations, *J. Geophys. Res.* **118,** 1122–1141, doi: 10.1002/jgrb.50094.

Sibson, R. H. (1973). Interactions between temperature and pore-fluid pressure during earthquake faulting and a mechanism for partial or total stress relief, *Nature Phys. Sci.* **243,** 66–68.

Simpson, R. W., M. Barall, J. Langbein, J. R. Murray, and M. J. Rymer (2006). San Andreas fault geometry in the Parkfield, California, region, *Bull. Seismol. Soc. Am.* **96,** no. 4B, S28–S37, doi: 10.1785/0120050824.

Tago, J., V. M. Cruz-Atienza, J. Virieux, V. Etienne, and F. J. Sánchez-Sesma (2012). A 3D hp-adaptive discontinuous Galerkin method for modeling earthquake dynamics, *J. Geophys. Res.* **117,** no. B09312, doi: 10.1029/2012JB009313.

Templeton, E. L., and J. R. Rice (2008). Off-fault plasticity and earthquake rupture dynamics: 1. Dry materials or neglect of fluid pressure changes, *J. Geophys. Res.* **113,** no. B09306, doi: 10.1029/2007JB005529.

Ulrich, T., and A.-A. Gabriel (2017). 3D fault curvature and fractal roughness: Insights for rupture dynamics and ground motions using a Discontinuous Galerkin method, *19th EGU General Assembly, EGU2017*, Vienna, Austria, 23–28 April 2017, p. 18,689, http://adsabs.harvard.edu/abs/2017EGUGA..1918689U (last accessed March 2018).

Wollherr, S., and A.-A. Gabriel (2016). Off-fault plasticity in dynamic rupture simulations: 3D numerical analysis and effects on rupture transfer in complex fault geometries (Poster 062), *Proc. of the 2016 Annual Meeting of the Southern California Earthquake Center*, Palm Springs, California, Vol. XXVI, 252–253.

Zhang, Z., W. Zhang, and X. Chen (2014). Three-dimensional curved grid finite-difference modelling for non-planar rupture dynamics, *Geophys. J. Int.* **199,** no. 2, 860–879, doi: 10.1093/gji/ggu308.

Ruth A. Harris
Brad Aagaard
U.S. Geological Survey
345 Middlefield Road, MS 977
Menlo Park, California 94025 U.S.A.
harris@usgs.gov

Michael Barall
Invisible Software Inc.
P.O. Box 6541
San Jose, California 95150 U.S.A.

Shuo Ma
Daniel Roten
Kim Olsen
Department of Geological Sciences
San Diego State University
San Diego, California 92182 U.S.A.

Benchun Duan
Dunyu Liu
Bin Luo
Department of Geological Sciences
Texas A&M University
College Station, Texas 77843 U.S.A.

Kangchen Bai
Jean-Paul Ampuero
California Institute of Technology
Seismological Laboratory
1200 E. California Boulevard
Pasadena, California 91125 U.S.A.

Yoshihiro Kaneko
GNS Science
P.O. Box 30-368

Lower Hutt 5040
New Zealand

Alice-Agnes Gabriel
Kenneth Duru
Thomas Ulrich
Stephanie Wollherr
Department of Earth and Environmental Sciences
Ludwig-Maximilians-Universität München
Theresienstrße 41
80333 Munich
Germany

Zheqiang Shi
Tokio Marine Technologies
2160 Satellite Boulevard, Suite 400
Duluth, Georgia 30097 U.S.A.

Eric Dunham
Sam Bydlon
Department of Geophysics
Stanford University
Stanford, California 94305 U.S.A.

Zhenguo Zhang
Xiaofei Chen
Department of Earth and Space Sciences
Southern University of Science and Technology
1088 Xueyuan Avenue, Shenzhen
Guangdong, China

Surendra Nadh Somala
Department of Civil Engineering
Indian Institute of Technology (IIT) Hyderabad
Kandi, Sangareddy
Telangana 502285, India

Christian Pelties
Munich Re
Fraunbergstraße 12
81379 Munich
Germany

Josué Tago
Facultad de Ingeniería
Universidad Nacional Autónoma de México
Mexico City, Mexico

Victor Manuel Cruz-Atienza
Instituto de Geofísica
Universidad Nacional Autónoma de México
Mexico City, Mexico

Jeremy Kozdon
Department of Applied Mathematics
Naval Postgraduate School
833 Dyer Road
Monterey, California 93943 U.S.A.

Eric Daub
Khurram Aslam
Center for Earthquake Research and Information
University of Memphis
3890 Central Avenue
Memphis, Tennessee 38152 U.S.A.

Yuko Kase
Geological Survey of Japan
National Institute of Advanced Industrial Science and Technology (AIST)
Tsukuba Central 7, Tsukuba
Ibaraki 305-8567, Japan

Kyle Withers
U.S. Geological Survey
P.O. Box 25046, MS 966
Denver, Colorado 80225 U.S.A.

Luis Dalguer
swissnuclear
Frohburgstrasse 20, P.O. Box 1663
CH-4601 Olten, Switzerland

Published Online 4 April 2018